frontiers | Frontiers in Earth Science

ORIGINAL RESEARCH
published: 20 June 2022
doi: 10.3389/feart.2022.882201

Sedimentary Rock Magnetic Response to Holocene Environmental Instability in the Pearl River Delta

Yi Wu[1,2,3,4]*, *Shuqing Fu*[1,2]*, *Haixian Xiong*[5], *Yongqiang Zong*[2,6], *Tingping Ouyang*[7], *Shasha Peng*[8], *Jianxin Cai*[1,3], *Yulin Han*[1,3] and *Zhaoyu Zhu*[4,8]

[1]Southern Marine Science and Engineering Guangdong Laboratory (Guangzhou), Guangzhou, China, [2]Key Lab of Guangdong for Utilization of Remote Sensing and Geographical Information System, Guangdong Open Laboratory of Geospatial Information Technology and Application, Guangzhou Institute of Geography, Guangdong Academy of Sciences, Guangzhou, China, [3]Key Laboratory of Ocean and Marginal Sea Geology, South China Sea Institute of Oceanology, Innovation Academy of South China Sea Ecology and Environmental Engineering, Chinese Academy of Sciences, Guangzhou, China, [4]State Key Laboratory of Loess and Quaternary Geology, Institute of Earth Environment, Chinese Academy of Sciences, Xi'an, China, [5]School of Marine Sciences, Sun Yat-sen University, Zhuhai, China, [6]Department of Earth Sciences, The University of Hong Kong, Hong Kong, Hong Kong SAR, China, [7]School of Geography, South China Normal University, Guangzhou, China, [8]State Key Laboratory of Isotope Geochemistry, CAS Center for Excellence in Deep Earth Science, Guangzhou Institute of Geochemistry, Chinese Academy of Sciences, Guangzhou, China

OPEN ACCESS

Edited by:
Xiting Liu,
Ocean University of China, China

Reviewed by:
Weiguo Zhang,
East China Normal University, China
Deming Kong,
Guangdong Ocean University, China

***Correspondence:**
Yi Wu
wuy@scsio.ac.cn
Shuqing Fu
fsq519@163.com

Specialty section:
This article was submitted to Quaternary Science, Geomorphology and Paleoenvironment, a section of the journal Frontiers in Earth Science

Received: *23 February 2022*
Accepted: *10 May 2022*
Published: *20 June 2022*

Citation:
Wu Y, Fu S, Xiong H, Zong Y, Ouyang T, Peng S, Cai J, Han Y and Zhu Z (2022) Sedimentary Rock Magnetic Response to Holocene Environmental Instability in the Pearl River Delta. Front. Earth Sci. 10:882201. doi: 10.3389/feart.2022.882201

Located on the northern coast of the South China Sea, the densely populated Pearl River Delta has experienced the combined effects of sea-level change, monsoon-driven discharge, and especially human activity, since the late Holocene. However, how these factors have regulated the regional environmental and sedimentary evolution remains unclear. To better understand these processes, we conducted a high-resolution rock magnetic investigation of the Holocene sediments of core DS01, drilled in the vicinity of the West River channel in the head area of the Pearl River deltaic plain. The magnetic grain-size proxy of the ARM/κ_{lf} ratio (the ratio of anhysteretic remanent magnetization to low-field magnetic susceptibility) indicates a long-term fining trend of the magnetite grain size, which may be a response to an increase in the weathering intensity in the Asian monsoon region during the Holocene. An interval with an enhanced concentration of magnetic minerals (mainly magnetite and hematite) occurred during 7.7–4.8 kyr BP (calendar years before 1950), coinciding with a period of delta progradation. During the marine transgression in the early Holocene, two similar intervals of magnetic enrichment may reflect regional hydrodynamic shifts associated with cooling events at ~9.5–9.3 kyr BP and 8.2 kyr BP. The subsequent 4.2 kyr BP cooling event possibly induced a cold and dry environment in the sediment source area. From ~800 yr BP onward, there was a major increase in the sedimentary magnetic mineral content, likely in response to intensified agricultural and industrial activities.

Keywords: environmental evolution, magnetic minerals, sea-level changes, cold events, human activity, Pearl River Delta

1 INTRODUCTION

The formation of the sedimentary sequences of the Pearl River (Zhu Jiang) Delta in southern China likely began in the late Quaternary (e.g., Huang et al., 1982; Zhao, 1990). Developed on the northern coast of the South China Sea, in an area undergoing long-term tectonic subsidence, the regional sedimentary sequences of the deltaic plain have documented the complex history of marine transgression and regression (e.g., Zong et al., 2009; Wei and Wu, 2011; Zong et al., 2012; Zong et al., 2016; Wei X. et al., 2020). The modern Pearl River Delta is a densely populated and industrialized area, which is strongly influenced by the Asian summer monsoon (An, 2000; An et al., 2000). Determining the environmental and sedimentary evolution of the Pearl River Delta is a complex task, especially during the Holocene, when human activities became an increasingly important influence. Stalagmite records from China have provided detailed information on the paleoclimatic evolution of the Asian monsoon over the last 640 kyr (Cheng et al., 2016). For the latest 10 kyr, from the early Holocene onward, precisely dated proxy environmental records are available, such as the stalagmite records from southern China (Yuan et al., 2004; Dykoski et al., 2005; Wang et al., 2005). The $\delta^{18}O$ record from Dongge Cave suggests a weakening trend of Asian monsoon intensity for most of the Holocene, which was punctuated by pronounced short-term monsoon events that can be correlated regionally or globally (Wang et al., 2005).

An integrated analysis of a transect of sediment cores recovered from along both sides of the current channel of the West River (Xi Jiang), a tributary extending west–east to the Pearl River catchment, has provided a Holocene record of the deltaic evolution of the head area of the Pearl River deltaic plain (**Figure 1**) (Xiong et al., 2018; Fu et al., 2020). Within the area, lithostratigraphic units deposited above bedrock can be

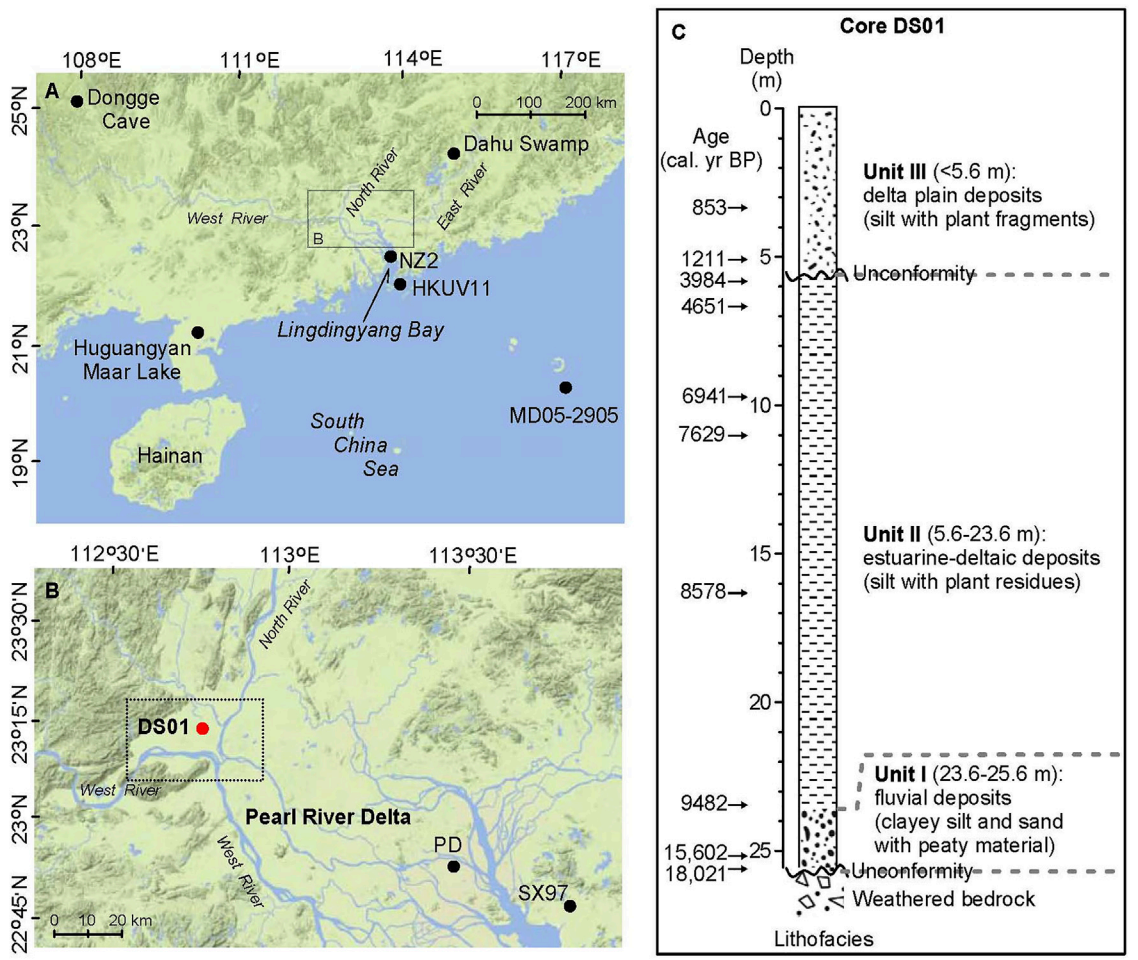

FIGURE 1 | Location map **(A,B)** and stratigraphic information **(C)** for sediment core DS01 (red circle) in the head area (dotted rectangle) of the Pearl River deltaic plain. Black circles mark the locations of sites discussed in the text: Dongge Cave (Wang et al., 2005), Dahu Swamp (Zhou et al., 2004), Huguangyan Maar Lake in south China (Wang et al., 2016), core HKUV11 (8.4 m water depth, Wu et al., 2017), core MD05-2905 (1,647 m water depth, Zhou et al., 2012) in the northern South China Sea, core NZ2 (4.6 m water depth) in Lingdingyang Bay (Pearl River estuary, Wu et al., 2021), and core PD and core SX97 from the banks of the Pearl River estuary (Yang et al., 2008; Peng et al., 2014). The 10 radiocarbon dates for core DS01 shown in **(C)** are from Fu et al. (2020). Details of the methods used to produce the age data are given in Xiong et al. (2018). The maps were produced using Tencent Map App.

subdivided into three major groups: fluvial deposits, estuarine-deltaic deposits, and delta plain deposits, with decreasing depth. These sedimentary facies correspond to different sedimentary environments in the head area of the Pearl River Delta, and they provide an opportunity to obtain a relatively complete regional paleoenvironmental record throughout the Holocene.

In this study, we investigated a Holocene sedimentary sequence from the Pearl River Delta using rock magnetic measurements, which have been widely used for paleoenvironmental reconstruction (Thompson and Oldfield, 1986; Evans and Heller, 2003; Liu et al., 2012). Originating from the adjacent terrigenous areas of the Pearl River drainage, the detrital magnetic minerals in the sediments can potentially be used to decipher the paleoenvironmental history of the drainage area. Rock magnetic results have been reported for various drilling sites in the Pearl River estuary (e.g., Yang et al., 2008; Peng et al., 2014; Wu et al., 2021) (**Figures 1A,B**). These studies have provided abundant information about the interplay of sea-level changes and sedimentary evolution in the coastal area since at least the late Pleistocene. In the present study, we measured multiple rock magnetic parameters, at high stratigraphic resolution, from a sediment core from the delta, with the aim of reconstructing millennial- to centennial-scale records of the Holocene sedimentary evolution of the head area of the Pearl River Delta. We compare the records with previous reconstructions of past regional climatic and environmental changes and attempt to understand how changes in climate, sea-level, and human impacts influenced the Holocene evolution of this coastal area.

2 MATERIALS AND METHODS

We used sediment core DS01 (**Figure 1B**; 23°13.47′N, 112°44.43′E; 25.61 m in length), obtained from the north side of the West River. The altitude of the coring site was ~4.4 m above the sea level. The base of the core consists of compact, reddish weathered bedrock. Above, the sediments can be divided into three lithological units, as illustrated in **Figure 1C**. An age of 18,181–17,865 cal. yr Before Present (BP) was obtained for a sand layer (within Unit I) that unconformably covered the base rock. The three units are described as follows: Unit I: (25.61–23.6 m), sand and clayey silt with occasional plant residues. Unit II (23.6–5.6 m), mainly dark silt with occasional plant residues; soft. This unit comprises the main part of the core. Unit III: (5.6–0 m), mainly gray silt with occasional plant fragments; loose structure. Fu et al. (2020) identified four subunits that should comprise a complete Unit III within the vicinity of the head area of the Pearl River Delta (**Figure 1**). However, in core DS01, two of these subunits are missing (sub-units IIIa and IIIb). Thus, we infer the existence of another sedimentary discontinuity between Unit II and Unit III.

Although not continuously represented in core DS01, the sedimentary succession in the study area was found to record a progressive transition from an estuarine to a deltaic environment, associated with the upper part of Unit II (**Figure 1C**). In this study, samples were collected every 2 cm by pressing plastic cubes ($2 \times 2 \times 2\ cm^3$) into the center of the archive half of core DS01. The surface sediments (upper ~110 cm) were not sampled to avoid sediments affected by recent agricultural and industrial activities. Another set of samples was collected at 10–20 cm intervals for analyses of grain size, organic carbon isotopes, and diatoms. These results were previously published (Xiong et al., 2018; Fu et al., 2020) and will be partially aiding the following discussions in our study.

Low-frequency (976 Hz) and high-frequency (15,616 Hz) volume magnetic susceptibilities (κ_{lf} and κ_{hf}, respectively) were measured on a total of 570 discrete cubic specimens (equivalent to a sampling resolution of 4.3 cm), using an AGICO Kappabridge MFK1-FA magnetic susceptibility meter. The volume frequency-dependent susceptibility (κ_{fd}) was calculated as $\kappa_{fd} = \kappa_{lf} - \kappa_{hf}$. κ_{lf} generally reflects the concentration of paramagnetic and ferromagnetic components, and κ_{fd} is sensitive to the presence of superparamagnetic grains (Thompson and Oldfield, 1986; Evans and Heller, 2003; Liu et al., 2012).

Anhysteretic remanent magnetization (ARM) was imparted in a peak alternating field (AF) of 100 mT with a direct current biasing field of 0.05 mT superimposed, using a 2G AF demagnetizer. ARM was measured using a 2G three-axis cryogenic superconducting rock magnetometer (755R) installed in a shielded room with residual fields of <300 nT, in the Paleomagnetism Laboratory of the South China Sea Institute of Oceanology, Chinese Academy of Sciences. ARM is sensitive to stable single-domain ferrimagnetic grains (e.g., ~40 nm for magnetite). We calculated the ARM/κ_{lf} ratio as a proxy for detecting relative changes in the grain size of magnetite (Banerjee et al., 1981; King et al., 1982).

Saturation isothermal remanent magnetization (SIRM) was imparted in a field of 1T using an ASC Impulse Magnetizer (IM-10-30) and measured using an AGICO JR-6A rock magnetometer. Back fields of 100 mT ($IRM_{-100\ mT}$) and 300 mT ($IRM_{-300\ mT}$) were then imparted and measured sequentially. Back IRMs were imparted to every third sample (n = 190). The SIRM and backfield IRMs are used to calculate hard IRM (HIRM) and *S*-ratio (Thompson and Oldfield, 1986; Evans and Heller, 2003) as follows:

$$HIRM = 0.5 \times (SIRM + IRM_{-300mT}),$$
$$S - ratio = -IRM_{-300mT}/SIRM.$$

SIRM mainly reflects the combined concentrations of ferrimagnetic (e.g., magnetite) and imperfect antiferromagnetic particles (e.g., hematite and goethite), predominantly the former, unless the magnetic mineral assemblages are dominated by imperfect antiferromagnetic material. HIRM and *S*-ratio are widely used as proxies for the absolute and relative concentrations of imperfect antiferromagnetic particles, respectively. The ARM/SIRM ratio was calculated as an additional magnetic grain-size proxy, since it is unaffected by paramagnetic and superparamagnetic minerals.

In addition to the aforementioned routine magnetic measurements, selected samples were used for the following more detailed magnetic measurements. High-temperature magnetic susceptibility measurements (κ_{lf}-T) were made on

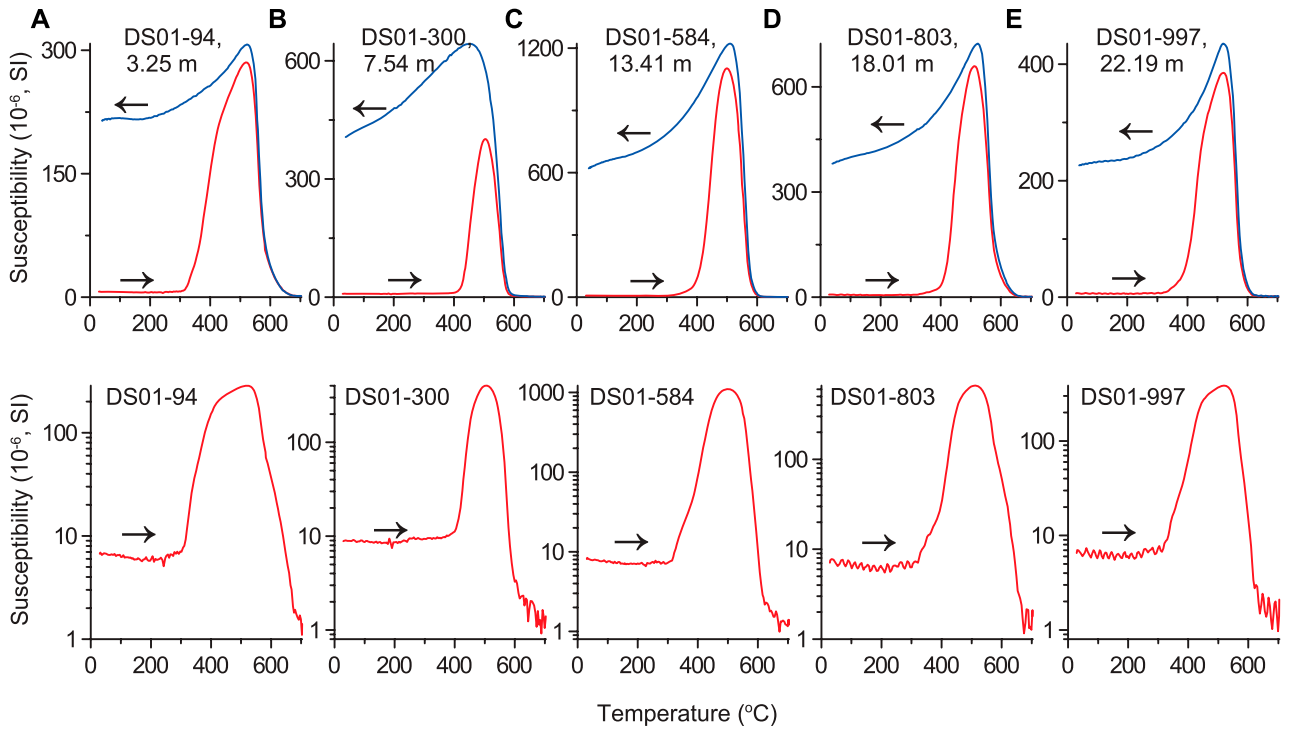

FIGURE 2 | Temperature-dependent magnetic susceptibility (κ_{lf}-T) curves for representative samples from core DS01. Arrows indicate heating (red) and cooling (blue) runs.

freeze-dried powder samples in an argon environment, using the Kappabridge MFK1-FA combined with a CS-4 high-temperature furnace. IRM acquisition curves were measured in magnetic fields ranging from 1 mT to 1.5 T (in 90 logarithmically distributed steps), followed by backfield demagnetization in a range of magnetic fields up to 100 mT. Hysteresis loops were obtained by cycling the magnetic field between ±1.0 T, with a step size of 5 mT. These measurements were made using a Lakeshore 8600 vibrating sample magnetometer (software version 1.3) at the Environmental Magnetism Laboratory of South China Normal University.

3 RESULTS

3.1 Magnetic Mineralogy

The thermomagnetic curves (κ_{lf}-T) of the five representative samples are largely consistent, showing a slight decrease in κ_{lf} from room temperature to ~300°C during heating (see the lower panel in **Figure 2**). This may be caused by the gradual unblocking of paramagnetic (or superparamagnetic) minerals, such as siderite and pyrite (Dunlop and Özdemir, 2001; Roberts, 2015). Above ~300°C, κ_{lf} begins to increase and a "hump" is evident between 400 and 550°C. The cooling limb of the curve is not reversible because stoichiometric ferrimagnetic minerals have been produced during heating, possibly from the thermally induced alteration of paramagnetic iron-bearing silicates and/or clays (e.g., Deng et al., 2001; Liu et al., 2020). All the curves show a sharp decrease near 580°C, the Curie temperature of magnetite, indicating that magnetite is likely the major magnetic carrier of the samples. The decreasing trend continues beyond 600°C, revealing the presence of a magnetic phase with a Curie temperature greater than that of magnetite. A weak convex pattern appears at ~120°C during each of the cooling runs, likely arising from the presence of a minor amount of goethite.

Figure 3A shows that the IRMs at 300 mT contribute ~73–88% to the SIRM values, with *S*-ratios ranging from 11.5 to 95.3%, with a ~61% median for the whole core (n = 192). The representative samples have a wide range of coercivities of remanence (~35–105 mT) (**Figure 3B**). We conclude that the dominant remanence carriers are low-coercivity ferrimagnetic minerals, but with high-coercivity phases being abundant.

The hysteresis loops of the selected samples are slightly wasp-waisted (**Figures 3C–G**), which may result from the coexistence of two different magnetic components with contrasting coercivities (Roberts et al., 1995; Tauxe et al., 1996). Furthermore, the loops are almost closed when approaching 600 mT, which also demonstrates the coexistence of both low- and high-coercivity magnetic components in the sediments.

3.2 Down-Core Variations in Magnetic Properties

Down-core plots of multiple magnetic parameters are presented in **Supplementary Figure S1**. Using the pre-existing age data for the core (**Figure 1C**), we built an age model based on linear

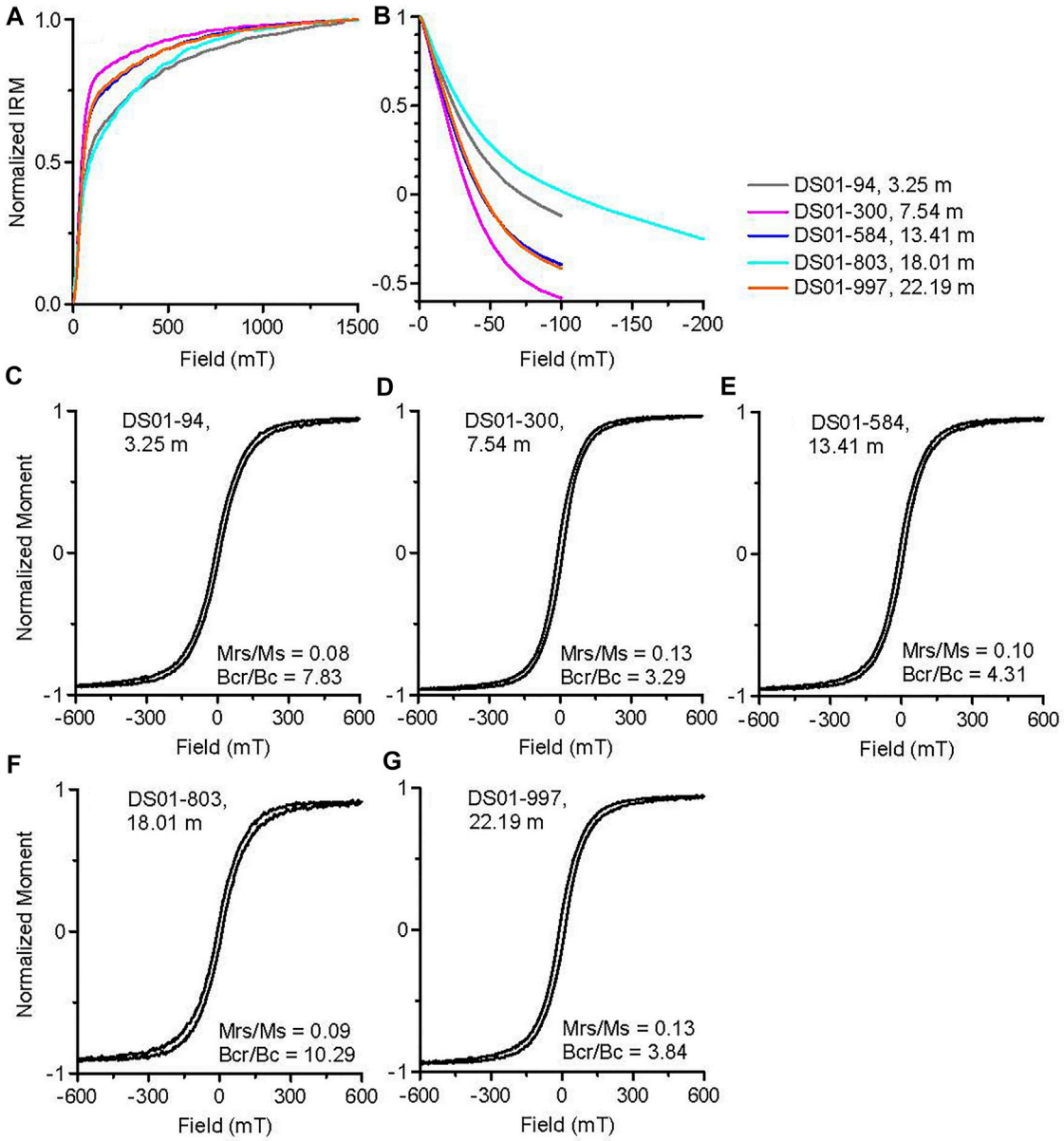

FIGURE 3 | IRM acquisition curves and backfield IRM curves **(A,B)** and hysteresis loops **(C–G)** for representative samples from core DS01. Ms, saturation magnetization; Mrs, saturation remanence; Bc, coercivity; Bcr, coercivity of remanence. Hysteresis loop data of the samples shown in **(C–F)** were processed using the HystLab program (Paterson et al., 2018).

interpolation or extrapolation (**Figure 4**). However, this was not possible for Unit I (25.6–23.6 m) because the evaluated ages for the upper part would be much younger than those of the base of Unit II, assuming a constant sedimentation rate (~16.5 cm/kyr) estimated from the pre-existing age data. We infer that Unit I was rapidly deposited in a high-energy freshwater environment. Two age data are available for Unit III, and they indicate a high sedimentation rate (~5 m/kyr) within the interval of 1308–420 yr BP, resulting in a clear age discrepancy between Unit III and Unit II. This sedimentary hiatus may have been caused by river channel migration or later human activities (Fu et al., 2020). Six age data are available for Unit II, and therefore the chronology for this lithologic unit is of a relatively high resolution.

Within Unit II, four horizons are highlighted due to the relatively high values of most of the magnetic parameters (**Supplementary Figure S1**, **Table 1** and **Figure 4**). Interval (a) (~22.0–23.6 m, ~9.3–9.5 kyr BP) is a plateau-like zone of the magnetic parameters, at the base of Unit II, corresponding to the period when an estuarine environment began to dominate in the study area. In interval (b), around the middle of Unit II, a minor peak is evident in almost all the magnetic parameter

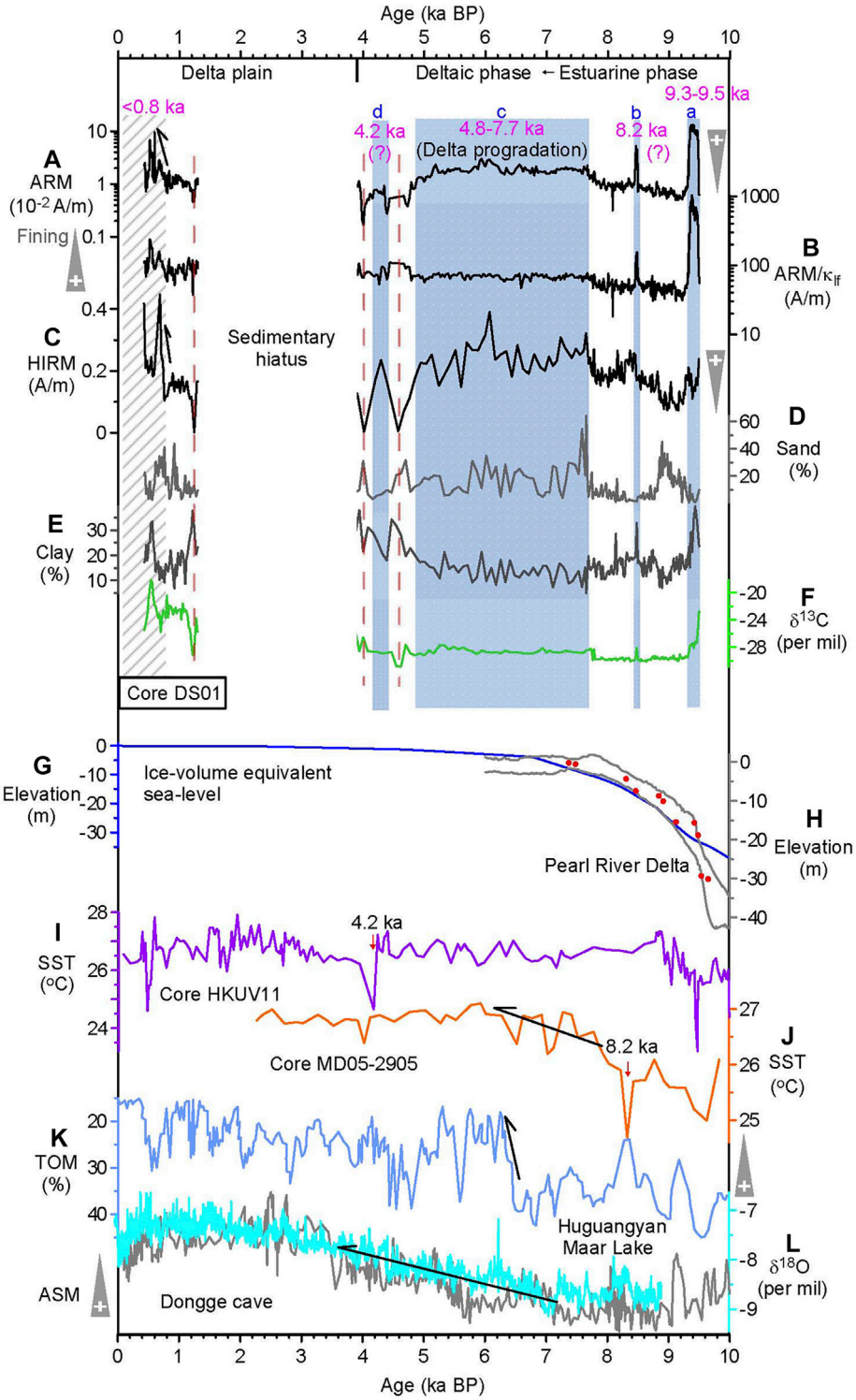

FIGURE 4 | Comparison of magnetic records for core DS01 with selected independent paleoenvironmental records. **(A–C)** ARM, ARM/κ_{lf}, and HIRM (this study); **(D–F)** sand content, clay content, and carbon isotope ratios ($\delta^{13}C$) from core DS01 (Fu et al., 2020); **(G)** elevations of ice-volume equivalent sea-level (Lambeck et al., 2014); **(H)** elevations from the mean sea level during 6–10 kyr BP, after correction for regional tectonic subsidence and sedimentary compaction [redrawn from Xiong et al. (2018)]; **(I,J)** sea surface temperature reconstructions from core HKUV11 (Wu et al., 2017) and core MD05-2905 (Zhou et al., 2012), respectively; **(K)** total organic matter (TOM) record from Huguangyan Maar Lake (Wang et al., 2016); and **(L)** the speleothem oxygen isotope record ($\delta^{18}O$ from Dongge Cave, an indicator of Asian summer monsoon intensity, ASM) (~0–9 kyr BP, cyan curve (Wang et al., 2005); 0–10 kyr BP, gray curve (Dykoski et al., 2005). In **(H)**, red circles represent corrected elevations (without range) from drilling cores from the Pearl River Delta head area and estuarine area, while the (upper and lower) gray curves represent the 99% probability envelope of the reconstructed sea-level changes across the Pearl River Delta.

TABLE 1 | Ranges of variation of the magnetic parameters for core DS01 and intervals (a–d).

	Core DS01		Interval a		Interval b		Interval c		Interval d	
	Mean	Max/min	Mean	Max/min	Mean	Max/min	Mean	Max/min	Mean	Max/min
κ_{lf} (10^{-6}, SI)	175.7	452.2 (25.5)	171.3	290.0 (91.4)	320.0	379.3 (219.7)	265.8	452.2 (58.5)	96.3	126.6 (62.6)
κ_{fd} (10^{-6}, SI)	2.9	28.6 (0.0)	6.9	19.1 (0.0)	5.7	12.1 (2.0)	3.5	8.1 (0.9)	2.1	8.1 (1.0)
ARM (10^{-2} A/m)	1.5	13.4 (0.2)	7.8	13.4 (0.6)	3.3	5.3 (1.1)	1.8	3.0 (0.5)	0.7	3.0 (0.5)
SIRM (A/m)	1.1	3.9 (0.0)	1.1	1.6 (0.6)	1.9	2.7 (0.7)	2.3	3.9 (0.5)	0.7	0.8 (0.5)
HIRM (A/m)	0.2	0.4 (0.0)	0.2	0.2 (0.1)	0.2	0.3 (0.2)	0.2	0.4 (0.1)	0.2	0.2 (0.2)
S-ratio (%)	59.8	95.3 (11.5)	68.0	81.1 (16.8)	71.2	84.9 (47.3)	77.7	84.2 (50.3)	42.6	50.7 (36.3)
ARM/κ_{lf} (A/m)	91.4	1042.4 (10.0)	480.5	1042.4 (53.8)	98.5	155.4 (48.1)	68.5	92.8 (46.8)	71.0	108.9 (52.9)
ARM/SIRM (10^{-2})	1.6	10.1 (0.7)	6.2	10.1 (0.9)	1.3	1.9 (0.9)	0.8	1.2 (0.7)	1.0	1.1 (1.0)

profiles. However, intervals (a) and (b) do not have comparably high HIRM values, which indicates the dominant contribution of ferrimagnetic minerals (magnetite) in these intervals. Except for intervals (a) and (b), Unit II shows increasing but slightly different values of the magnetic parameters, including κ_{lf}, ARM, SIRM, HIRM, *S*-ratio, and ARM/κ_{lf} (**Supplementary Figures S1C,E–J**). Therefore, these trends did not develop simultaneously. Within interval (c), κ_{lf}, ARM, SIRM, HIRM, and *S*-ratio fluctuate within an interval of overall higher values. Interval (d), at the top of Unit II, is characterized by rapid changes in most of the magnetic parameters, with HIRM showing a significant peak, indicating a peak in the concentration of hard magnetic components (mainly hematite). In contrast, there are only minor peaks in κ_{lf}, ARM, and SIRM.

There is a general upward-increasing trend in ARM/κ_{lf}, as shown in **Supplementary Figure S1I**, suggesting the progressive fining of the magnetic grains (mainly magnetite). The ARM/SIRM ratio shows relatively uniform values throughout most of the core, with no comparable fluctuations in the interval of 11.3–6.8 m [interval (c)], but with an increase thereafter (**Supplementary Figure S1J**).

Cross-plots showing the relationships between the magnetic parameters are shown in **Supplementary Figure S2**. For κ_{lf}, κ_{fd}, ARM, and SIRM (**Supplementary Figures S2A–C,F**, respectively) linear relationships are evident for most of the data, indicating a general consistency of the sedimentary magnetic assemblages; deviations in these linear relationships generally correspond to high-amplitude fluctuations of the respective parameters within the profiles. κ_{fd} was not expected to be closely related with both ARM and SIRM (**Supplementary Figures S2D,E**) as they are indicative of distinctive magnetic-domain states; however, the data points in both plots are generally clustered, as the magnetic minerals are seemingly concentrated within sedimentary intervals with a higher clay content (**Figure 4**).

3.3 Hard Isothermal Remanent Magnetization and *S*-Ratio

The rock magnetic results show that magnetite and hematite are the dominant magnetic minerals in core DS01 and that the parameters related to magnetic mineral concentration (κ_{lf}, ARM, SIRM, HIRM, and *S*-ratio) show very similar stratigraphic patterns. The depositional context of the core location varied substantially since ~18 kyr BP, and the material sources of the core sediments may have undergone substantial changes. This inference may undermine the use of HIRM and *S*-ratio, as they may be significantly affected by changes in magnetic mineral coercivity. Therefore, we used the *L*-ratio of Liu et al. (2007) to evaluate if these parameters were influenced by Al-substituted hematite or goethite, or both, since this would result in a wide range of coercivities which would invalidate their use. The *L*-ratio is calculated as follows:

$$L - \text{ratio} = \text{HIRM} / [0.5\times\ (\text{SIRM} + \text{IRM}_{-100\text{mT}})].$$

Reference to **Figure 5A** shows a nearly constant distribution for most of the data points. The outliers are related to the specific sediment layers in **Figure 5B** and **Figure 4** and coincide with the transitional interval from Unit II to Unit III (**Supplementary Figure S1**), during which the depositional environment was very unstable. The horizontally shaded intervals in **Figure 5B** are characterized by magnetic minerals with substantially different coercivities, which may reflect different sources; hence, the use of HIRM and *S*-ratio may be inappropriate in these intervals. However, in the other intervals, both parameters can be used to quantify the absolute and relative concentrations of high-coercivity magnetic minerals (Liu et al., 2007; Roberts et al., 2020).

4 DISCUSSION

The magnetic properties of sedimentary archives are often correlated with geological processes that control the provenance, transportation, deposition, and post-depositional modification (e.g., diagenesis) of sediments. The thermomagnetic analyses suggest a relatively uniform sedimentary magnetic mineral composition (**Figure 2**), likely suggesting a consistent sediment source. This inference is supported by the generally consistent coercivities of the magnetic minerals indicated by the *L*-ratio (**Figure 5**), as well as by the similar hysteresis loops of the representative samples (**Figures 3C–G**). However, there are significant fluctuations in magnetic mineral concentration and in magnetic grain size, as shown by the stratigraphic variations of κ_{lf}, ARM, SIRM, HIRM, and *S*-ratio and by the magnetic grain-size indicators, ARM/κ_{lf} and ARM/SIRM. We now focus on these fluctuations, especially on the intervals of enhanced magnetic concentration and their potential paleoenvironmental implications.

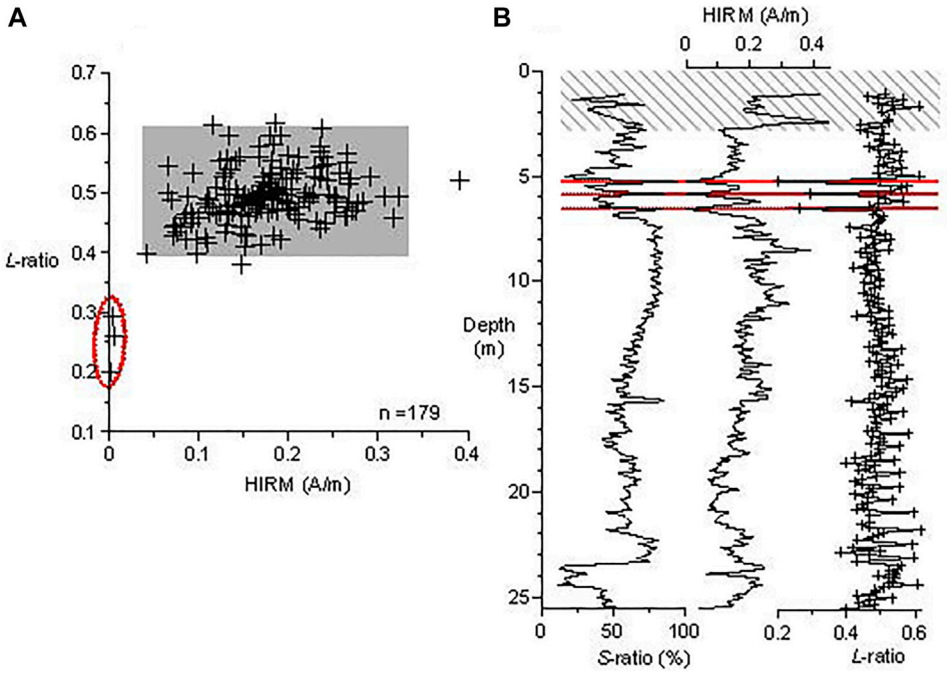

FIGURE 5 | Relationship between *L*-ratio and HIRM, and down-core variations of *S*-ratio, HIRM, and *L*-ratio. Red dotted lines (in **B**) indicate three depths with low values in the *L*-ratio profile, referring to symbols plotted within the red-dotted ellipse (in **A**).

4.1 Episodes of Magnetic Mineral Enrichment

Intervals (a–d) in Unit II are dated to ~9.5–9.3 kyr BP, 8.5–8.4 kyr BP, 7.7–4.8 kyr BP, and 4.4–4.2 kyr BP, respectively, while the uppermost part of the core may provide a record of the last ~800 yr (**Figure 4**, **Table 1**). Intervals (a), (b), and (d) in core DS01 correspond to three short Bond-like cooling events (Bond et al., 1997; Bond et al., 2001) that are recorded in the stalagmite record from Dongge Cave, in southern China, in which more enriched $\delta^{18}O$ values represent intervals of a weakened monsoon (**Figure 4L**). These rapid events may be dynamically linked to climate changes in the North Atlantic and Greenland (Dykoski et al., 2005; Wang et al., 2005). The linkage may be related to the strengthening of the Siberia High, which significantly affects the East Asian monsoon climate (Chen et al., 1991; Ding et al., 1995; Liu and Ding, 1998).

Intervals (a), (b), and (c) in core DS01 correspond to enhanced concentrations of both hard and soft magnetic components (**Figure 4**, **Table 1**, and **Supplementary Figure S1**). These intervals are related to quite different regional environments in terms of the degree of marine influence, representing the transition from an estuarine to a deltaic environment in the head area of the Pearl River Delta (**Figure 1**). In contrast, interval (d), at the top of Unit II, is characterized by a higher concentration of imperfect antiferromagnetic minerals. Combined with the evaluation of the HIRM and *S*-ratio records (below), we infer that interval (d) represents a cold climatic event, similar to interval (b); however, the two intervals may be the product of different fluvial processes and depositional environments. The uppermost part of the core may predominantly reflect anthropogenic influences, rather than natural processes.

4.1.1 Possible Brief Climatic Events at 9.5–9.3, 8.5–8.4, and 4.4–4.2 Thousand Years Before Present

During the early Holocene, the entire Pearl River Delta likely experienced a rapid sea-level rise (**Figure 4H**). Xiong et al. (2018) found that the rates of sea-level rise around the southeast coast of China doubled from 10.5 to 9.5 kyr BP, increasing from 16 to 33 mm/yr. Global sea-level changes, reconstructed from fluctuations in global ice volume, show a near-uniform rise during ~11.4–8.4 kyr BP (**Figure 4G**, Lambeck et al., 2014). Core DS01 contains a prominent peak in the concentration of magnetic minerals after 9.5 kyr BP. At this time, the head area of the Pearl River Delta may have become an intertidal environment, corresponding to the lower part of Unit II (**Figures 1B,C**). Therefore, the site location of core DS01 would have been strongly influenced by the marine transgression at ~9.5 kyr BP. Subsequently, rapid sediment accumulation occurred at the core site, including fine-grained sediments. Interval (a) is well-defined in most of the magnetic profiles (**Supplementary Figure S1**) and has a comparable level of magnetic enhancement to interval (b). In both zones, there is a pronounced increase in the clay content and a corresponding low sand content (**Figures 4D,E**). Evidently, these fine-grained sediments had higher concentrations of magnetic minerals than the coarse fraction. Thus, the magnetic properties and bulk sediment grain size suggest that these two intervals represent an abrupt shift in hydrodynamic forces that may have been associated with changes in precipitation and runoff

in the river catchment during a period of weakened summer monsoon intensity.

Within the limits of the age model, intervals (b) (8.5–8.4 kyr BP) and (d) (4.4–4.2 kyr BP) are potentially correlative with the Holocene cooling events on the centennial scale, at ~8.2 and 4.2 kyr BP, respectively. The magnetic parameters (**Supplementary Figure S1**), bulk sediment grain size, and carbon isotope ratios (**Figure 4**) collectively display coherent variations corresponding to intervals (a) and (b). By contrast, interval (d) is characterized by an increase in HIRM, hence showing an increase in the hematite content. This may reflect a cold, dry climate and oxidizing conditions in the source area. In a deltaic environment with a limited marine influence, the core site was likely subjected to weak hydrodynamic sorting during this interval (**Figures 4D,F**). Adjacent sediment core HKUV11 likely recorded a rapid cooling event at ~4.2 kyr BP (**Figure 4I**; Wu et al., 2017), while core MD05-2905 from the northern South China Sea recorded an abrupt temperature decrease at ~8.2 kyr BP (**Figure 4J**; Zhou et al., 2012). However, there is no corresponding cooling signal in the global sea-level record (**Figure 4G**, Lambeck et al., 2014). In southernmost mainland China, the total organic matter content of the sediments of Huguangyan Maar Lake recorded cooling events at 8.2 kyr BP and 9.2 kyr BP (**Figure 4K**). Several other short-term cold/dry events are also evident in proxy environmental records from Holocene lake sediments from the region, including the 4.2 kyr BP cold event (Wang et al., 2016).

4.1.2 Environmental Changes During 7.7–4.8 Thousand Years Before Present

The diatom-derived salinity record (**Supplementary Figure S1K**) indicates that during the interval of 7.7–4.8 kyr BP, following the early–middle Holocene marine transgression, the study site experienced delta progradation and the accumulation of terrestrial sediments (or a marine regression) (Zong et al., 2012; Zong et al., 2016; Xiong et al., 2018; Fu et al., 2020). Reconstructions of the Holocene sea-level history in the Pearl River Delta show that the sea level was approximately stable during the last 7 kyr (Zong et al., 2012; Xiong et al., 2018). The diatom profile suggests that the head area of the Pearl River Delta experienced a reduced marine influence during this interval (**Supplementary Figure S1K**), which may be associated with the initiation of widespread sedimentation in the Pearl River deltaic basin (**Figure 4**). Sediments that were sourced from tropical and subtropical areas and had undergone intensive weathering were deposited in the basin area, leading to the overall sedimentary magnetic enhancement throughout this interval.

4.1.3 Environmental Changes Since ~800 Years Before Present

Recent agricultural and industrial activities, such as cultivation, deforestation, and mining, may have accelerated the production of magnetic minerals in Earth surface sediments. Organic carbon isotope records ($\delta^{13}C$) from at least two drilling cores (including core DS01) from the head area of the Pearl River Delta reveal a general enrichment trend in the uppermost sedimentary unit (Fu et al., 2020). Numerous previous studies have provided evidence of agricultural activity in the Pearl River Delta since at least 2.5–2.2 kyr BP (e.g., Zong et al., 2010; Yang et al., 2012; Hu et al., 2013). Although the uppermost part of the core was not sampled for magnetic measurements, there is a pronounced increase in the contents of hematite and fine-grained magnetite since ~800 yr BP (**Figures 4A,C**), which is approximately coeval with the mid-Southern Song Dynasty. This interval corresponds to the peak period of Medieval warmth, represented in terrestrial climatic reconstructions (Mann et al., 2008). These changes in the magnetic profiles of core DS01 may be the result of intensified human activities in the Pearl River catchment, rather than to the phase of deltaic development over the area. Based on speleothem records, Zhang et al. (2008) hypothesized a close linkage between changes in monsoonal climate and Chinese cultural phases. A rapid increase in human disturbance from ~900 yr BP is evident in the As record from a sediment core from the south of Hainan Island (Wan et al., 2015). The provision of high-resolution chronologies for the late Quaternary sediments of the study area remains challenging (e.g., Yim, 1999); moreover, there may be uncertainties in correlating records of monsoon intensity and rainfall, as argued by Zhang et al. (2010). Further research is needed to precisely determine the contribution of human activities to the properties of the recent sediments of the study area.

4.2 Regional Environmental Changes in the Context of the Evolution of the East Asian Summer Monsoon

4.2.1 Holocene Climatic Optimum

The period before interval (c) (~7.7–4.8 kyr BP) corresponds to the early Holocene marine transgression and is regarded as the climatic optimum in East Asia. Early studies proposed quite different timings for the Holocene optimum (defined as the peak in monsoonal precipitation or effective moisture) across the domain of the East Asian summer monsoon: at ~3 kyr BP in southern China and at ~9 kyr BP in northern China (see An et al., 2000 and references therein). Zhou et al. (2022) proposed a gradual northward expansion of the Holocene optimum in the East Asian monsoon region (from 24.25°N to 48.74°N), based on pollen-based precipitation reconstructions. A depleted early Holocene stalagmite $\delta^{18}O$ signal is evident at Dongge Cave (**Figure 4L**), which likely indicates a wetter Asian summer monsoon climate, as the $\delta^{18}O$ record of Dongge Cave is anticorrelated with the Asian summer monsoon intensity (Wang et al., 2005). Records of pollen (Zhou et al., 2004) and bulk organic carbon isotope ratios (Zhong et al., 2010) from Dahu Swamp, to the north of the East River in the Pearl River drainage (**Figure 1**), suggest a pronounced warm and wet period during the early Holocene (~10–6 kyr BP), which may be related to a strengthened East Asian summer monsoon. Wei Z. et al. (2020) conducted sedimentary magnetic analyses at Dahu Swamp and proposed a rainfall maximum during the mid-Holocene (~8–4 kyr BP). Although the magnetic record differs from other paleoenvironmental reconstructions from Dahu Swamp,

the magnetic record is in phase with an equivalent record from Daping Swamp (26°10.18′N, 110°08′E), to the north-west of Dahu Swamp (Zhong et al., 2018). Both locations may be sensitive to local hydrological changes as they are in hydrologically closed lake basins (Zhong et al., 2018; Wei Z. et al., 2020). Huguangyan Maar Lake (**Figure 1**) may record the earliest timing of the Holocene optimum, as indicated by an elevated total organic matter content during 11.5–6.5 kyr BP (Wang et al., 2016). A pollen record from the lake sediments indicated that during the early Holocene (11.6–7.8 kyr BP), the area was dominantly occupied by trees and shrubs, with tropical trees recording maximum percentages during ~9.5–8.0 kyr BP (Wang et al., 2007). Thus, there may be minor offsets in the timing of the climatic optimum between the reconstructions from Huguangyan Maar Lake and Dahu Swamp. However, it is possible to conclude that, at least in southeastern China, the Holocene climatic optimum was not significantly time-transgressive and that the Holocene optimum undoubtedly occurred during the early Holocene. In the vicinity of the site of core DS01, a rapid marine transgression occurred during this period, which was associated with relatively low and uniform magnetic mineral concentrations, except the interval (a) (**Figure 4**).

4.2.2 Long-Term Trend of Environmental Evolution

Both magnetic grain-size parameters in core DS01 (**Supplementary Figures S1I,J**) show no clear response to either marine transgression or regression, when compared, for example, with the salinity profile (**Supplementary Figure S1K**). This is quite different from the records from core SX97 (Peng et al., 2014) or core PD (Yang et al., 2008), which recorded frequent oscillations during the late Quaternary or Holocene. The ARM/κ_{lf} ratio in core DS01 indicates the long-term fining of the magnetic grain size, except for the lower part of the core (below ~22 m). Neither of the neighboring cores shows comparable trends in their magnetic records (Yang et al., 2008; Peng et al., 2014; Wu et al., 2021). Seaward of the Pearl River estuary, the magnetic grains within the surface sediments become increasingly fine, which likely resulted from the dissolution of superparamagnetic grains (Ouyang et al., 2017). An increasing distance from the source areas could also result in a fining of the magnetic grain size, as finer grains are likely to be transported longer distances than coarser grains (Huang et al., 2021). However, this is not applicable here, as indicated by the *L*-ratio (**Figure 5**). It is unlikely that sea-level changes were responsible for the long-term fining trend of magnetic grains evident in core DS01, although there is a close relationship between sea-level changes and sedimentary magnetic grain-size variations in the South China Sea (see Kissel et al., 2020 and references therein). Neither is there clear evidence for the effect of sea-level change on East Asian monsoon intensity (e.g., Wang et al., 2001). We tentatively attribute the magnetic grain-size trend to a slightly increasing weathering intensity in the material source areas. Within the East Asian monsoon domain, the monsoonal climate (as a source of heat and moisture) would be expected to be a major factor controlling erosion and weathering processes in the Pearl River catchment. In comparison, there was a long-term trend of decreasing monsoon precipitation in southern China since the early Holocene (**Figure 4L**; Dykoski et al., 2005; Wang et al., 2005), which does not necessarily conflict with increased weathering during the same period because of the complex regional hydrothermal conditions. Additionally, sediment pore water may have affected the magnetic measurements. Since water is generally diamagnetic and the sedimentary water content generally decreases down-core, ARM/κ_{lf} could be biased accordingly. However, this influence is likely to be minor, as the pore-water content was relatively low.

5 SUMMARY

We have obtained a high-resolution rock magnetic record for drilling core DS01 to reconstruct the Holocene environmental evolution of the Pearl River Delta. The results indicate a relatively uniform magnetic mineral assemblage. A sedimentary hiatus occurred during ~3.9–1.3 kyr BP. Enhanced magnetic mineral concentrations have occurred at the top of the core since ~800 yr BP, which we attribute to the intensified anthropogenic impact. The ARM/κ_{lf} ratio indicates a long-term trend of decreasing magnetite grain size during the Holocene, which may be a response to intensified weathering in the East Asian monsoon region. However, we cannot exclude the influence of residual pore water on this trend. A prominent interval of increased magnetic mineral concentration occurred during ~7.7–4.8 kyr BP, associated with delta progradation (or marine regression) in the study area. Three abrupt shifts in magnetic properties occurred at ~9.5–9.3, ~8.5–8.4, and ~4.4–4.2 kyr BP, which are potentially correlated with Bond-like events. The two older events are coeval with the initiation of the Holocene optimum in southeastern China, while the youngest event occurred in the context of deltaic development and minimal direct marine influence. It should be noted that possible uncertainties in the age model of core DS01 hinder the definitive correlation of these events with records from elsewhere, and further investigations of the Holocene sedimentary sequences in the Pearl River Delta and adjacent regions of East Asian monsoon influence are needed.

DATA AVAILABILITY STATEMENT

New data from this study are available from the Mendeley Data (http://dx.doi.org/10.17632/wcdhtstwtc.1).

AUTHOR CONTRIBUTIONS

YW and SF conceived the study and collected sub-samples for measurements; HX conducted the core drilling; YZ initiated the study on the Pearl River Delta; YW, YH, and JC conducted environmental magnetic analyses; TO and SP performed the rock magnetic analyses; and YW wrote the manuscript with input

from SF, HX, ZZ, and TO. All co-authors contributed to discussion and approved the submitted version.

FUNDING

This work was supported financially by grants from the Key Special Project for Introduced Talents Team of Southern Marine Science and Engineering Guangdong Laboratory (Guangzhou) (No. GML2019ZD0204), the Guangdong Basic and Applied Basic Research Foundation (Nos. 2019A1515011488 and 2017A030311020), the Guangdong Academy of Sciences (Nos. 2016GDASRC-0209 and 2020GDASYL-20200401001), and the Open Foundation of State Key Laboratory of Loess and Quaternary Geology at the Institute of Earth Environment, CAS (No. SKLLQG1838).

ACKNOWLEDGMENTS

We thank Qunshu Tang for helpful discussions during the preparation of the manuscript, Yuemin Lin and Mingkun Li for assistance with rock magnetic analyses performed at South China Normal University, and Jan Bloemendal for language polishing. We thank the Associate Editor (Xiting Liu) and the reviewers for constructive comments that helped to improve the article.

SUPPLEMENTARY MATERIAL

The Supplementary Material for this article can be found online at: https://www.frontiersin.org/articles/10.3389/feart.2022.882201/full#supplementary-material

REFERENCES

An, Z., Porter, S. C., Kutzbach, J. E., Wu, X., Wang, S., Xiaodong, S., et al. (2000). Asynchronous Holocene Optimum of the East Asian Monsoon. *Quat. Sci. Rev.* 19 (8), 743–762. doi:10.1016/S0277-3791(99)00031-1

An, Z. (2000). The History and Variability of the East Asian Paleomonsoon Climate. *Quat. Sci. Rev.* 19 (1-5), 171–187. doi:10.1016/S0277-3791(99)00060-8

Banerjee, S. K., King, J., and Marvin, J. (1981). A Rapid Method for Magnetic Granulometry with Applications to Environmental Studies. *Geophys. Res. Lett.* 8, 333–336. doi:10.1029/gl008i004p00333

Bond, G., Kromer, B., Beer, J., Muscheler, R., Evans, M. N., Showers, W., et al. (2001). Persistent Solar Influence on North Atlantic Climate during the Holocene. *Science* 294 (5549), 2130–2136. doi:10.1126/science.1065680

Bond, G., Showers, W., Cheseby, M., Lotti, R., Almasi, P., DeMenocal, P., et al. (1997). A Pervasive Millennial-Scale Cycle in North Atlantic Holocene and Glacial Climates. *Science* 278 (5341), 1257–1266. doi:10.1126/science.278.5341.1257

Chen, L. X., Zhu, J. G., and Lou, H. B. (1991). *Monsoons over East Asia*. Beijing: Meteorology Press. (in Chinese).

Cheng, H., Edwards, R. L., Sinha, A., Spötl, C., Yi, L., Chen, S., et al. (2016). The Asian Monsoon Over the Past 640,000 Years and Ice Age Terminations. *Nature* 534 (7609), 640–646. doi:10.1038/nature18591

Deng, C., Zhu, R., Jackson, M. J., Verosub, K. L., and Singer, M. J. (2001). Variability of the Temperature-Dependent Susceptibility of the Holocene Eolian Deposits in the Chinese Loess Plateau: A Pedogenesis Indicator. *Phys. Chem. Earth Part A* 26, 873–878. doi:10.1016/S1464-1895(01)00135-1

Ding, Z., Liu, T., Rutter, N. W., Yu, Z., Guo, Z., and Zhu, R. (1995). Ice-Volume Forcing of East Asian Winter Monsoon Variations in the Past 800,000 Years. *Quat. Res.* 44 (2), 149–159. doi:10.1006/qres.1995.1059

Dunlop, D. J., and Özdemir, Ö. (2001). *Rock Magnetism: Fundamentals and Frontiers*. New York: Cambridge University Press.

Dykoski, C., Edwards, R., Cheng, H., Yuan, D., Cai, Y., Zhang, M., et al. (2005). A High-Resolution, Absolute-Dated Holocene and Deglacial Asian Monsoon Record from Dongge Cave, China. *Earth Planet. Sci. Lett.* 233 (1-2), 71–86. doi:10.1016/j.epsl.2005.01.036

Evans, M. E., and Heller, F. (2003). *Environmental Magnetism: Principles and Applications of Enviromagnetic*. San Diego: Academic Press.

Fu, S., Xiong, H., Zong, Y., and Huang, G. (2020). Reasons for the Low Sedimentation and Slow Progradation in the Pearl River Delta, Southern China, during the Middle Holocene. *Mar. Geol.* 423, 106133. doi:10.1016/j.margeo.2020.106133

Hu, D., Clift, P. D., Böning, P., Hannigan, R., Hillier, S., Blusztajn, J., et al. (2013). Holocene Evolution in Weathering and Erosion Patterns in the Pearl River Delta. *Geochem. Geophys. Geosyst.* 14 (7), 2349–2368. doi:10.1002/ggge.20166

Huang, J., Jiao, W., Liu, J., Wan, S., Xiong, Z., Zhang, J., et al. (2021). Sediment Distribution and Dispersal in the Southern South China Sea: Evidence from Clay Minerals and Magnetic Properties. *Mar. Geol.* 439, 106560. doi:10.1016/j.margeo.2021.106560

Huang, Z. G., Li, P. R., Zhang, Z. Y., Li, K. H., and Qiao, P. N. (1982). *Formation, Development and Evolution of the Zhujiang Delta*. Guangzhou: Science and Technology Press of Guangzhou.

King, J., Banerjee, S. K., Marvin, J., and Özdemir, Ö. (1982). A Comparison of Different Magnetic Methods for Determining the Relative Grain Size of Magnetite in Natural Materials: Some Results from Lake Sediments. *Earth Planet. Sci. Lett.* 59, 404–419. doi:10.1016/0012-821X(82)90142-X

Kissel, C., Laj, C., Jian, Z., Wang, P., Wandres, C., and Rebolledo-Vieyra, M. (2020). Past Environmental and Circulation Changes in the South China Sea: Input from the Magnetic Properties of Deep-Sea Sediments. *Quat. Sci. Rev.* 236, 106263. doi:10.1016/j.quascirev.2020.106263

Lambeck, K., Rouby, H., Purcell, A., Sun, Y., and Sambridge, M. (2014). Sea Level and Global Ice Volumes from the Last Glacial Maximum to the Holocene. *Proc. Natl. Acad. Sci. U.S.A.* 111 (43), 15296–15303. doi:10.1073/pnas.1411762111

Liu, C., Wang, W., and Deng, C. (2020). A New Weathering Indicator from High-Temperature Magnetic Susceptibility Measurements in an Argon Atmosphere. *Geophys. J. Int.* 221, 2010–2025. doi:10.1093/gji/ggaa128

Liu, Q., Roberts, A. P., Larrasoaña, J. C., Banerjee, S. K., Guyodo, Y., Tauxe, L., et al. (2012). Environmental Magnetism: Principles and Applications. *Rev. Geophys* 50 (4), RG4002. doi:10.1029/2012rg000393

Liu, Q., Roberts, A. P., Torrent, J., Horng, C., and Larrasoaña, J. C. (2007). What Do the HIRM and *S*-Ratio Really Measure in Environmental Magnetism? *Geochem. Geophys. Geosyst.* 8 (9), Q09011. doi:10.1029/2007gc001717

Liu, T., and Ding, Z. (1998). Chinese Loess and the Paleomonsoon. *Annu. Rev. Earth Planet. Sci.* 26 (1), 111–145. doi:10.1146/annurev.earth.26.1.111

Mann, M. E., Zhang, Z., Hughes, M. K., Bradley, R. S., Miller, S. K., Rutherford, S., et al. (2008). Proxy-Based Reconstructions of Hemispheric and Global Surface Temperature Variations Over the Past Two Millennia. *Proc. Natl. Acad. Sci. U.S.A.* 105 (36), 13252–13257. doi:10.1073/pnas.0805721105

Ouyang, T., Li, M., Appel, E., Fu, S., Jia, G., Li, W., et al. (2017). Magnetic Properties of Surface Sediments from the Pearl River Estuary and its Adjacent Waters: Implication for Provenance. *Mar. Geol.* 390, 80–88. doi:10.1016/j.margeo.2017.06.002

Paterson, G. A., Zhao, X., Jackson, M., and Heslop, D. (2018). Measuring, Processing, and Analyzing Hysteresis Data. *Geochem. Geophys. Geosyst.* 19 (7), 1925–1945. doi:10.1029/2018gc007620

Peng, J., Yang, X., Huang, W., and Su, Z. (2014). Sea-level Fluctuations and Response to Global Changes during the Holocene in the Pearl River Delta, South China. *Acta Sci. Nat. Univertitatis Sunyatseni* 53 (6), 63–72. (in Chinese with English abstract). doi:10.13471/j.cnki.acta.snus.2014.06.008

Roberts, A. P., Cui, Y., and Verosub, K. L. (1995). Wasp-Waisted Hysteresis Loops: Mineral Magnetic Characteristics and Discrimination of Components in Mixed Magnetic Systems. *J. Geophys. Res.* 100, 17909–17924. doi:10.1029/95jb00672

Roberts, A. P. (2015). Magnetic Mineral Diagenesis. *Earth-Sci. Rev.* 151, 1–47. doi:10.1016/j.earscirev.2015.09.010

Roberts, A. P., Zhao, X., Heslop, D., Abrajevitch, A., Chen, Y., Hu, P., et al. (2020). Hematite (α-Fe_2O_3) Quantification in Sedimentary Magnetism: Limitations of Existing Proxies and Ways Forward. *Geosci. Lett.* 7, 8. doi:10.1186/s40562-020-00157-5

Tauxe, L., Mullender, T. A. T., and Pick, T. (1996). Potbellies, Wasp-Waists, and Superparamagnetism in Magnetic Hysteresis. *J. Geophys. Res.* 101 (B1), 571–583. doi:10.1029/95jb03041

Thompson, R., and Oldfield, F. (1986). *Environmental Magnetism*. London: Allen & Unwin.

Wan, S., Toucanne, S., Clift, P. D., Zhao, D., Bayon, G., Yu, Z., et al. (2015). Human Impact Overwhelms Long-Term Climate Control of Weathering and Erosion in Southwest China. *Geology* 43 (5), 439–442. doi:10.1130/g36570.1

Wang, S., Lü, H., Liu, J., and Negendank, J. F. W. (2007). The Early Holocene Optimum Inferred from a High-Resolution Pollen Record of Huguangyan Maar Lake in Southern China. *Chin. Sci. Bull.* 52 (20), 2829–2836. doi:10.1007/s11434-007-0419-2

Wang, X., Chu, G., Sheng, M., Zhang, S., Li, J., Chen, Y., et al. (2016). Millennial-Scale Asian Summer Monsoon Variations in South China Since the Last Deglaciation. *Earth Planet. Sci. Lett.* 451, 22–30. doi:10.1016/j.epsl.2016.07.006

Wang, Y., Cheng, H., Edwards, R. L., He, Y., Kong, X., An, Z., et al. (2005). The Holocene Asian Monsoon: Links to Solar Changes and North Atlantic Climate. *Science* 308 (5723), 854–857. doi:10.1126/science.1106296

Wang, Y. J., Cheng, H., Edwards, R. L., An, Z. S., Wu, J. Y., Shen, C.-C., et al. (2001). A High-Resolution Absolute-Dated Late Pleistocene Monsoon Record from Hulu Cave, China. *Science* 294 (5550), 2345–2348. doi:10.1126/science.1064618

Wei, X., Wu, C., Cai, S., and Zhan, W. (2020). Long-Term Morphodynamic Evolution of the Pearl River Delta from the Perspective of Energy Flux and Dissipation Changes. *Quat. Int.* 553, 118–131. doi:10.1016/j.quaint.2020.05.047

Wei, X., and Wu, C. (2011). Holocene Delta Evolution and Sequence Stratigraphy of the Pearl River Delta in South China. *Sci. China Earth Sci.* 54 (10), 1523–1541. doi:10.1007/s11430-011-4238-6

Wei, Z., Zhong, W., Xue, J., Ouyang, J., Shang, S., Ye, S., et al. (2020). Late Quaternary East Asian Summer Monsoon Variability Deduced from Lacustrine Mineral Magnetic Records of Dahu Swamp, Southern China. *Paleoceanogr. Paleoclimatol.* 35 (2), e2019PA003796. doi:10.1029/2019pa003796

Wu, M.-S., Zong, Y., Mok, K.-M., Cheung, K.-M., Xiong, H., and Huang, G. (2017). Holocene Hydrological and Sea Surface Temperature Changes in the Northern Coast of the South China Sea. *J. Asian Earth Sci.* 135, 268–280. doi:10.1016/j.jseaes.2017.01.004

Wu, Y., Fu, S., and Xia, Z. (2021). Magnetic Variations of Sediments from a Drilling Core in the Lingdingyang Bay, Zhujiang River Estuary, and Their Responses to Marine Transgression and Regression. *Haiyang Xuebao* 43 (5), 88–99. (in Chinese with English abstract). doi:10.12284/hyxb2021059

Xiong, H., Zong, Y., Qian, P., Huang, G., and Fu, S. (2018). Holocene Sea-Level History of the Northern Coast of South China Sea. *Quat. Sci. Rev.* 194, 12–26. doi:10.1016/j.quascirev.2018.06.022

Yang, S., Zheng, Z., Huang, K., Zong, Y., Wang, J., Xu, Q., et al. (2012). Modern Pollen Assemblages from Cultivated Rice Fields and Rice Pollen Morphology: Application to a Study of Ancient Land Use and Agriculture in the Pearl River Delta, China. *Holocene* 22 (12), 1393–1404. doi:10.1177/0959683612449761

Yang, X., Grapes, R., Zhou, H., and Yang, J. (2008). Magnetic Properties of Sediments from the Pearl River Delta, South China: Paleoenvironmental Implications. *Sci. China Ser. D-Earth Sci.* 51 (1), 56–66. doi:10.1007/s11430-007-0151-4

Yim, W. W.-S. (1999). Radiocarbon Dating and the Reconstruction of Late Quaternary Sea-Level Changes in Hong Kong. *Quat. Int.* 55 (1), 77–91. doi:10.1016/S1040-6182(98)00029-9

Yuan, D., Cheng, H., Edwards, R. L., Dykoski, C. A., Kelly, M. J., Zhang, M., et al. (2004). Timing, Duration, and Transitions of the Last Interglacial Asian Monsoon. *Science* 304 (5670), 575–578. doi:10.1126/science.1091220

Zhang, D., Li, H.-C., Ku, T.-L., and Lu, L. (2010). On Linking Climate to Chinese Dynastic Change: Spatial and Temporal Variations of Monsoonal Rain. *Chin. Sci. Bull.* 55 (1), 77–83. doi:10.1007/s11434-009-0584-6

Zhang, P., Cheng, H., Edwards, R. L., Chen, F., Wang, Y., Yang, X., et al. (2008). A Test of Climate, Sun, and Culture Relationships from an 1810-Year Chinese Cave Record. *Science* 322 (5903), 940–942. doi:10.1126/science.1163965

Zhao, H. (1990). *Evolution of the Pearl River Estuary*. Beijing: Ocean Press.

Zhong, W., Wei, Z., Shang, S., Ye, S., Tang, X., Zhu, C., et al. (2018). A 15,400-Year Record of Environmental Magnetic Variations in Sub-Alpine Lake Sediments from the Western Nanling Mountains in South China: Implications for Palaeoenvironmental Changes. *J. Asian Earth Sci.* 154, 82–92. doi:10.1016/j.jseaes.2017.12.005

Zhong, W., Xue, J., Cao, J., Zheng, Y., Ma, Q., Ouyang, J., et al. (2010). Bulk Organic Carbon Isotopic Record of Lacustrine Sediments in Dahu Swamp, Eastern Nanling Mountains in South China: Implication for Catchment Environmental and Climatic Changes in the Last 16,000 Years. *J. Asian Earth Sci.* 38 (3-4), 162–169. doi:10.1016/j.jseaes.2009.12.011

Zhou, B., Zheng, H., Yang, W., Taylor, D., Lu, Y., Wei, G., et al. (2012). Climate and Vegetation Variations since the LGM Recorded by Biomarkers from a Sediment Core in the Northern South China Sea. *J. Quat. Sci.* 27 (9), 948–955. doi:10.1002/jqs.2588

Zhou, W., Yu, X., Jull, A. J. T., Burr, G., Xiao, J. Y., Lu, X., et al. (2004). High-Resolution Evidence from Southern China of an Early Holocene Optimum and a Mid-Holocene Dry Event during the Past 18,000 Years. *Quat. Res.* 62 (1), 39–48. doi:10.1016/j.yqres.2004.05.004

Zhou, X., Zhan, T., Tu, L., Smol, J. P., Jiang, S., Liu, X., et al. (2022). Monthly Insolation Linked to the Time-Transgressive Nature of the Holocene East Asian Monsoon Precipitation Maximum. *Geology* 50 (3), 331–335. doi:10.1130/g49550.1

Zong, Y., Huang, G., Li, X. Y., and Sun, Y. Y. (2016). Late Quaternary Tectonics, Sea-Level Change and Lithostratigraphy along the Northern Coast of the South China Sea. *Geol. Soc. Spec. Publ.* 429 (1), 123–136. doi:10.1144/sp429.1

Zong, Y., Huang, K., Yu, F., Zheng, Z., Switzer, A., Huang, G., et al. (2012). The Role of Sea-Level Rise, Monsoonal Discharge and the Palaeo-Landscape in the Early Holocene Evolution of the Pearl River Delta, Southern China. *Quat. Sci. Rev.* 54, 77–88. doi:10.1016/j.quascirev.2012.01.002

Zong, Y., Yim, W. W.-S., Yu, F., and Huang, G. (2009). Late Quaternary Environmental Changes in the Pearl River Mouth Region, China. *Quat. Int.* 206 (1-2), 35–45. doi:10.1016/j.quaint.2008.10.012

Zong, Y., Yu, F., Huang, G., Lloyd, J. M., and Yim, W. W.-S. (2010). Sedimentary Evidence of Late Holocene Human Activity in the Pearl River Delta, China. *Earth Surf. Process. Landf.* 35 (9), 1095–1102. doi:10.1002/esp.1970

Conflict of Interest: The authors declare that the research was conducted in the absence of any commercial or financial relationships that could be construed as a potential conflict of interest.

Publisher's Note: All claims expressed in this article are solely those of the authors and do not necessarily represent those of their affiliated organizations, or those of the publisher, the editors, and the reviewers. Any product that may be evaluated in this article, or claim that may be made by its manufacturer, is not guaranteed or endorsed by the publisher.